



Research Article

Synthesis, crystallography, and conducting properties of a new nickel(II) complex containing 4-(diphenylamino)benzaldehyde-4-(ethyl)thiosemicarbazone

W. M. Zulhilmi W. M. Kharul Anwar^a, Uwaisulqarni M Osman^{a,*}, Maisara Abdul Kadir^a, Khadijah Hilmun Kamarudin^a, Mohd Ikmar Nizam Mohamad Isa^b, Suhana Arshad^c, Siti Nabilla Aliya Mohd Nizar^c

^aAdvanced Nano Materials Research Group (ANOMA), Ionic State Analysis (ISA), Laboratory, Faculty of Science and Marine Environment, Universiti Malaysia Terengganu, Kuala Nerus, Terengganu, 21030, Malaysia

^bEnergy Materials Consortium (EMC), Advanced Materials Team, Ionic & Kinetic Materials Research Laboratory (IKMaR), Faculty of Science & Technology, Universiti Sains Islam Malaysia, Nilai, Negeri Sembilan Darul Khusus, 71800, Malaysia

^cX-ray Crystallography Unit, School of Physics, Universiti Sains Malaysia, Pulau Pinang, 11800, Malaysia

ARTICLE INFO

Keywords:

Crystal structure
Ionic conduction
Ni(II) complex
Thiosemicarbazone

ABSTRACT

A new Nickel(II) complex, NiL₂, was prepared in this study by reacting 4-(diphenylamino)benzaldehyde-4-(ethyl)thiosemicarbazone and nickel(II) acetate. The resulting NiL₂ complex was thoroughly characterized by a variety of methods, such as elemental analysis, fourier transform infrared (FTIR) spectroscopy, ultraviolet-visible (UV-Vis) spectroscopy, magnetic susceptibility, and molar conductivity measurements. The material was also analyzed using a single-crystal X-ray diffraction (SCXRD) to identify its structural characteristics. FTIR confirmed that the ligand was bound to Ni(II) in a mononegative bidentate fashion through the azomethine (N=C) and thione sulfur (C=S) donor atoms. The UV-Vis spectrum and the measured magnetic moment are consistent with a diamagnetic species ($\mu_{\text{eff}} \approx 0$ BM), indicating a square planar geometry, which was confirmed by X-ray crystallographic data. The structural analysis showed a distorted square planar geometry with bond angle deviations up to 6°. The complex crystallized in the triclinic P-1 space group and adopted the thione tautomeric form. Moreover, NiL₂ was used as a dopant in solid biopolymer electrolyte (SBE) films prepared by the solution-casting technique using carboxymethyl cellulose (CMC) as the polymer host, polyethylene glycol (PEG) as a plasticizing agent, and isophthalic acid (IA) as the protonator. The highest ionic conductivity of 4.60×10^{-7} S cm⁻¹ at 353 K was achieved with CMC (1 g) + PEG (0.1 mL) + NiL₂ (15 wt%) + IA (20 wt%) of the SBE composition. In addition, the conductivity follows the Arrhenius behavior with an activation energy (E_a) of 0.144 eV, indicating that it requires low thermal energy to activate the charge carrier.

1. Introduction

Thiosemicarbazone derivatives have attracted the attention of many researchers due to their numerous benefits. The material is known for its thione sulfur (C=S) and azomethine (C=N) components, which can be chelated with metal to form a coordination complex compound that can enhance the properties of thiosemicarbazone derivatives (Gaber *et al.*, 2021). Most studies on thiosemicarbazone derivatives have focused on their biological activity, such as pharmaceutical, toxicological, and catalytic, while their electrical conductivity has received comparatively less attention (Rathinam *et al.*, 2024; Khan *et al.*, 2022). Thiosemicarbazone derivatives play a role in conductivity due to their N, S-donor, which can chelate with metal complexes while facilitating electron transfer within the system (Hassan *et al.*, 2024). The electronic properties of the N, S-donor ligands in combination with the variety of substituents that the system can form make the thiosemicarbazone ligand an effective chelating agent (Sarker *et al.*, 2020). Thus, chelation with metal complexes such as Ni(II) can increase the material's conductivity properties due to the transfer of electron pairs from the thiosemicarbazone ligand to the *d*-orbital of the Ni(II) ion.

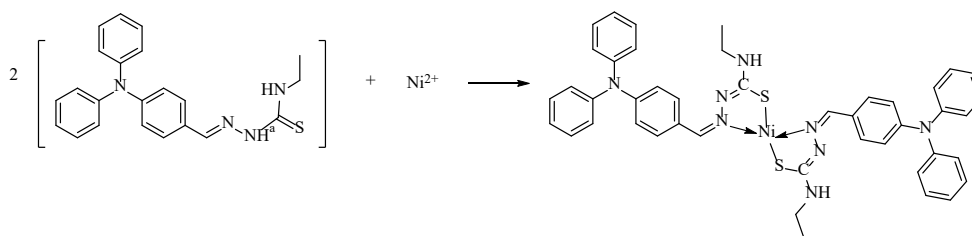
This interaction leads to a splitting of the *d*-orbitals, due to repulsion between ligand donor electrons and the *d*-orbital electrons of Ni(II), causing a separation of the energy levels (Chen *et al.*, 2022; Lococciolo *et al.*, 2024). This splitting of the *d*-orbitals can facilitate the electronic transitions within the metal complex and increase the mobility of the electrons, and hence their electrical conductivity (Tamer *et al.*, 2023). Many studies on the conductivity of Ni(II) complexes have shown that the conductivity properties of the materials are strongly affected by various factors. For example, a report on the ionic conductivity of Ni(II) dissolved in ethylene glycol showed values in the range of 0.75 – 7.61 S cm⁻¹ (Phi *et al.*, 2022). Other studies have shown that the introduction of metal into ligands can further improve their electrical properties. The complexation of the ligand leads to coordination with the metal, enhances intermolecular interactions and helps to increase their electrical conductivity (El-Shekeil *et al.*, 2010; Alam *et al.*, 2018). Moreover, the introduction of Ni(II) ions into a thiosemicarbazone ligand also led to an improvement in conductivity when used in solid biopolymer electrolytes (SBEs) (Osman *et al.*, 2020). This is particularly important in the context of SBEs, where the ionic conductivity must

*Corresponding author:

E-mail address: uwais@umt.edu.my (U.M. Osman)

Received: 18 February, 2025 Accepted: 15 December, 2025 Epub Ahead of Print: 18 February, 2026 Published: 24 February, 2026

DOI: 10.25259/JKSUS_382_2025

Scheme 1. Synthesis of NiL₂ complex.

be sufficiently high to enable practical applications (Sohaimy and Isa, 2022).

This study is a continuation of our recent publication on the synthesis of 4-(diphenylamino)benzaldehyde-4-(ethyl)thiosemicarbazone (Anwar et al., 2025), and we have extended our studies to the synthesis of metal complexes by reaction with Ni(II) ions. The conductivity of the resulting complex as a dopant in SBES is also to be evaluated in this study.

2. Materials and Methods

2.1 Materials

All chemicals employed in this research were purchased from BDH (British Drug Houses), Acros, and Fluka. Elementar Unicube elemental analyzer (Elementar Analysensystem GmbH, Germany) was used to perform the elemental analysis. A Johnson Matthey Mark I MSB magnetic susceptibility balance, model MKIC, was used to measure magnetic susceptibility. The molar conductivity was measured using a Jenway 4320 conductivity meter fitted with a platinumized electrode immersion cell. The UV spectrophotometer Shimadzu UV-1800 was used to record electronic absorption spectra, and the samples were prepared as 1.0×10^{-5} M solutions in dimethyl sulfoxide (DMSO).

2.2 Synthesis of NiL₂ complex

The NiL₂ complex was synthesized by refluxing 0.6 mmol of 4-(diphenylamino)benzaldehyde-4-(ethyl)thiosemicarbazone with 0.3 mmol of nickel(II) acetate in 40 mL of hot ethanol over a period of three hours under open-air conditions. After the reaction was complete, a dark brown precipitate was obtained, which was filtered, washed thoroughly with cold ethanol, and dried in a desiccator. Single crystals of the NiL₂ complex were produced using vapor diffusion, where a solution of the crude product was allowed to evaporate in a mixture of methanol and DMF in a ratio of 2:3 for 2 weeks until well-formed crystals were obtained. The general conversion has been illustrated in Scheme 1.

2.3 Single X-ray crystallography

A NiL₂ single crystal was placed on the goniometer, and diffraction data were measured at 296(2) K on a Bruker APEX II DUO CCD area-detector with MoK α radiation ($\lambda = 0.71073 \text{ \AA}$) with both ϕ and ω scans. A combination of all frames produced 26,225 reflections, of which 4,862 were independent (41.8% with $I > 2\sigma(F^2)$). The multi-scan absorption correction was performed through SADABS 2014/5 (Krause et al., 2014). The structure was solved by direct methods in SHELXTL (Bruker, 2009), and full-matrix least-squares refinement on F^2 was performed in SHELXTL (Sheldrick, 2014) using anisotropic displacement parameters on non-hydrogen atoms. SADABS (Bruker, 2009) was also used to correct diffraction intensities, and PLATON (Bruker, 2009) was utilized to perform geometric calculations. In addition, SHELXP (Bruker, 2009) was used to produce molecular graphics. Hydrogen atoms were positioned, calculated, and refined isotropically using a riding model, with Uiso fixed to 1.5 times the Ueq on terminal sp^3 carbons and 1.2 times the Ueq on all other carbon-bound hydrogens. Data quality and refinement statistics are as follows: $R_{\text{int}} = 0.1066$, $R_{\sigma} = 0.1165$, $R_1 = 0.0633$, $wR(F^2) = 0.1831$, and $S = 0.991$, with the largest residual electron density peak and hole of 0.26 and -0.33 e \AA^{-3} , respectively.

2.4 Preparation of the film and conductivity measurements using electrochemical impedance spectroscopy (EIS)

The solution-casting method was used to prepare polymer electrolyte films. To start with, 1 g of carboxymethylcellulose (CMC) and 0.1 mL of polyethylene glycol (PEG) were dissolved in 20 mL of distilled water. The NiL₂ dopant and isophthalic acid (IA) were added to this homogeneous solution in different proportions (0-25 wt% each) and stirred until dissolved. The mixture was subsequently poured into Petri dishes and dried in an oven at 55-60°C to produce thin films. The thickness of the dried film was measured with a micrometer at several points on each film, and the average value was used to calculate the conductivity. Then, the dried films were cut into 2 cm diameter discs and pressed between two stainless steel electrodes under spring pressure. These electrode assemblies were then attached to a HIOKI 3532-50 LCR Hi-tester to perform electrochemical impedance spectroscopy (EIS). The impedance was measured at room temperature and between 303 and 353 K, and the ionic conductivity (σ) of the NiL₂-doped films was determined by the following equation (Ramlli et al., 2022):

$$\sigma = \frac{t}{AxR_b} \quad (1)$$

Where t denotes the film thickness (cm), R_b is the bulk resistance determined from the intercept of X-axis of the Nyquist plot, and A represents the contact area between the film and the electrode. The activation energy (E_a) can be obtained by fitting the temperature dependence of the ionic conductivity to the Arrhenius equation (Ramlli et al., 2022):

$$\sigma = \sigma_0 \exp \frac{-E_a}{KT} \quad (2)$$

Where σ_0 denotes the pre-exponential factor, k is the Boltzmann constant, and T represents the absolute temperature in Kelvin.

3. Results and Discussion

3.1 Synthesis

In theory, the free ligand (LH) is predominantly present in the thione form, but when coordinated with Ni²⁺, deprotonation occurs, and the ligand converts to the thiolate form, which then binds to the Ni²⁺ metal center. The complexation was prepared by direct reactions between Ni²⁺ and LH in a molar ratio of 1:2, which corresponds to the chemical formula of NiL₂. The average yield was $87.48\% \pm 3.37\%$ when repeated five times, and the melting point was 201.5°C. The calculated elemental composition for C₄₄H₄₂N₈NiS₂ was C 65.43%, H 5.49%, N 13.87%, and S 7.94%, whereas the experimental analysis gave C 65.93%, H 4.94%, N 13.00%, and S 7.78%. The acceptable difference between the experimental and calculated Carbon, Hydrogen, Nitrogen and Sulphur (CHNS) values (<1%), indicates that the complex formed has a ratio of 1:2 ratio (metal:ligand) and is consistent with the proposed molecular formula, C₄₄H₄₂N₈NiS₂ (NiL₂). The NiL₂ complex was found to be diamagnetic at ambient temperature with an experimental magnetic moment of ≈ 0.00 BM. This lack of unpaired electrons in the split d -orbitals verifies a square planar geometrical arrangement around the nickel center (Osman et al., 2021). Moreover, the molar conductivity values of $13.7 \text{ S cm}^2 \text{ mol}^{-1}$ in 1×10^{-3} M DMSO solutions indicate a non-

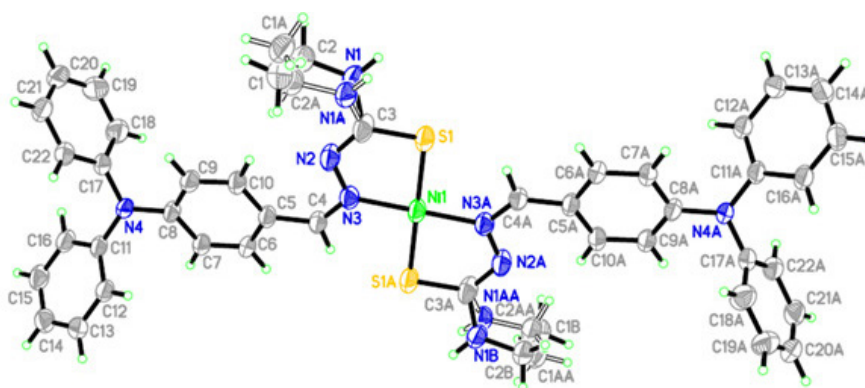


Fig. 1. ORTEP structure of NiL_2 complex showing 50% probability ellipsoids.

electrolytic behavior comparable to previous reports (Ekennia et al., 2019).

3.2 Infrared spectra

The FT-IR spectrum of the present NiL_2 dopant has been provided in Fig. S1 and is compared with its similar free ligand (Anwar et al., 2025) to study the binding mode. The FT-IR spectrum of the free ligand shows a band in the 1322 cm^{-1} region, which is assigned to the thioamide bands $\nu(\text{C}=\text{S})$ (Anwar et al., 2025). However, this band disappeared and a new band attributed to $\nu(\text{C}-\text{S})$ appeared at 639 cm^{-1} in NiL_2 . The peak for the functional group $\nu(\text{NH}^a)$ was absent in the NiL_2 dopant due to deprotonation of $-\text{SH}$ by tautomerism (Hassan et al., 2024), while it appeared in the free ligand at 3157 cm^{-1} (Anwar et al., 2025). Moreover, the $\nu(\text{CH}=\text{N})$ band shifted to a lower frequency (1578 cm^{-1}) upon complexation, compared to 1684 cm^{-1} for the free ligand (Anwar et al., 2025). The shift to a lower frequency is due to the $\text{C}=\text{N}$ bond becoming weaker, as the electron density around the nitrogen atom has been transferred to the $\text{Ni}(\text{II})$ ion (Lavanya et al., 2021). Thus, the FT-IR spectrum of NiL_2 confirmed the free ligand was coordinated through the azomethine nitrogen and the thione sulfur donor atoms. All other bands have appeared at the expected peaks, as previously reported (Farooq et al., 2024; Seifunnisha et al., 2021; Tarai et al., 2023).

3.3 Electronic spectra

The UV-Vis spectrum of the NiL_2 dopant (Fig. S2) was measured in DMSO. The UV-Vis spectrum of the NiL_2 dopant is very similar in shape to that of the similar free ligand (Anwar et al., 2025) and differs only in the values of the molar extinction coefficient (ϵ). In similar to the free ligand, two distinct peaks are observed at 299 nm ($21,700\text{ L mol}^{-1}\text{cm}^{-1}$) and 369 nm ($31,700\text{ L mol}^{-1}\text{cm}^{-1}$), which correspond to the $\pi \rightarrow \pi^*$ and $n \rightarrow \pi^*$ transitions of the conjugated triphenylamine and the lone pairs in the nitrogen and sulfur atoms (Anwar et al., 2025). In comparison, the UV-Vis spectrum of the NiL_2 dopant also shows two peaks at 301 nm ($\epsilon = 45,300\text{ L mol}^{-1}\text{cm}^{-1}$) and 395 nm ($88,700\text{ L mol}^{-1}\text{cm}^{-1}$) but at slightly higher absorption peak values than the free ligand, as seen in many previous reports (Zhang et al., 2024; Muthuramalingam et al., 2019).

Three bands for the ${}^1\text{A}_{1g} \rightarrow {}^1\text{A}_{2g}$, ${}^1\text{A}_{1g} \rightarrow {}^1\text{B}_{1g}$ and ${}^1\text{A}_{1g} \rightarrow {}^1\text{E}_g$ transitions were expected at $400\text{--}600\text{ nm}$ for diamagnetic and square planar of $\text{Ni}(\text{II})$ ions, but due to the strong inter-ligand transition, these transitions are obscured and result in a weak shoulder in this region (Zangrando et al., 2015). Thus, a new shoulder band appeared at 445 nm in the present NiL_2 doping, which can be assigned to the metal-ligand charge transfer transition (MLCT) indicating the complexation occurred (Arafath et al., 2023).

3.4 ${}^1\text{H}$ NMR

The ${}^1\text{H}$ NMR spectrum of the diamagnetic NiL_2 dopant (Fig. S3) shows similar peaks to those reported for its free ligand (Anwar et al., 2025). However, the peaks are shifted upfield, with a maximum shift of 2.07 ppm (Table S1), due to coordination with diamagnetic metal atoms (Rajeev A. et al., 2024), supporting the formation of the NiL_2 complex.

Additionally, the proton signal appears for one unit of ligand (L) due to the symmetric environment coordinated to the nickel(II) centre. The NH^a signal disappears due to deprotonation. The $\text{CH}=\text{N}$ proton is strongly deshielded because it is close to an electron-withdrawing nitrogen atom and appears as a singlet peak at $\delta_{\text{H}} = 9.77\text{ ppm}$, followed by a triplet peak at $\delta_{\text{H}} = 7.71\text{--}7.73\text{ ppm}$ for the NH proton. The aromatic ring protons appear at $\delta_{\text{H}} = 6.81\text{--}8.01\text{ ppm}$ as multiple peaks. The most weakly deshielded are the $-\text{CH}_2-$ and $-\text{CH}_3$ protons, which appear at $\delta_{\text{H}} = 3.21\text{--}3.14$ and $\delta_{\text{H}} = 1.09\text{--}1.05\text{ ppm}$, respectively.

3.5 Crystal structure of NiL_2

The solid-state molecular arrangement of the dopant was unambiguously determined by single-crystal X-ray diffraction. Comprehensive crystallographic parameters, along with refinement details, are compiled in Table S2. Whereas Table S3 provides the experimental bond lengths and angles. The dopant crystallized in the low-symmetry triclinic P-1 space group, where its asymmetric units assemble through intermolecular interactions to form a continuous three-dimensional network (Fig. 1). Each asymmetric unit consists of two molecules of the deprotonated ligand (L) and the crystallographically independent $\text{Ni}(\text{II})$ ion. The $\text{Ni}(\text{II})$ ion adopts a tetracoordinated NiN_2S_2 core with a square planar geometry that is slightly distorted, as reflected by the τ_4 value of 0.107 (10.7°), which lies much closer to the ideal square-planar limit ($\tau_4 = 0$) than the tetrahedral limit ($\tau_4 = 1$). In the NiN_2S_2 coordination core, Ni^{2+} is coordinated to two N-atoms (N3, N3A) and S-atoms (S1, S1A) of bidentate ligands, leading to the formation of two five-membered chelate rings. The deviation of the ideal square planar geometry can be seen in the bond angles: S1-Ni1-N3 ($85.84(11)^\circ$), N3-Ni1-S1A ($94.16(11)^\circ$), S1A-Ni1-N3A ($85.84(11)^\circ$) and N3A-Ni1-S1 ($94.16(11)^\circ$), which deviated slightly from the ideal 90° , similar as previous report (Biswas et al., 2024). The bond lengths for Ni1-N3 , Ni1-N3A , Ni1-S1 and Ni1-S1A were $1.898(3)$, $1.898(3)$, $2.1276(13)$, and $2.1276(13)\text{ \AA}$, respectively, which are consistent with other distorted square planar geometries of $\text{Ni}(\text{II})$ complexes (Osman et al., 2021).

The neighboring NiL_2 chains are connected by the $\text{C2A-H2AB} \cdots \text{S1A}$ and $\text{C12A-H12B} \cdots \text{S1A}$, forming a 3D scaffold structure with parallel layers along the b axis (Fig. 2). A summary of all observed hydrogen bonding geometries can be seen in Table S4. In addition, the crystal packing is further stabilized by $\pi \cdots \pi$ stacking interactions involving $\text{Cg1} \cdots \text{Cg3}$ [symmetry code: $1-x, -y, 1-z$] and $\text{Cg2} \cdots \text{Cg3}$ [symmetry code: $1+x, y, z$] contacts, both with centroid-centroid distances of $3.710(2)\text{ \AA}$. Here, Cg1 corresponds to the five-membered chelate ring (Ni1-S1-C3-N2-N3), Cg2 to its symmetry-related counterpart ($\text{Ni1-S1A-C3A-N2A-N3A}$) and Cg3 to the aromatic ring ($\text{C5-C6-C7-C8-C9-C10}$). Thus, the existence of intermolecular hydrogen bonds and $\pi \cdots \pi$ stacking interactions acts as a driving force in supramolecular compositions and crystal stability (Fig. 3).

3.6 Conductivity analysis

The impedance measurements were performed on CMC-PEG films with different concentrations of NiL_2 dopant (system 1) and IA (system

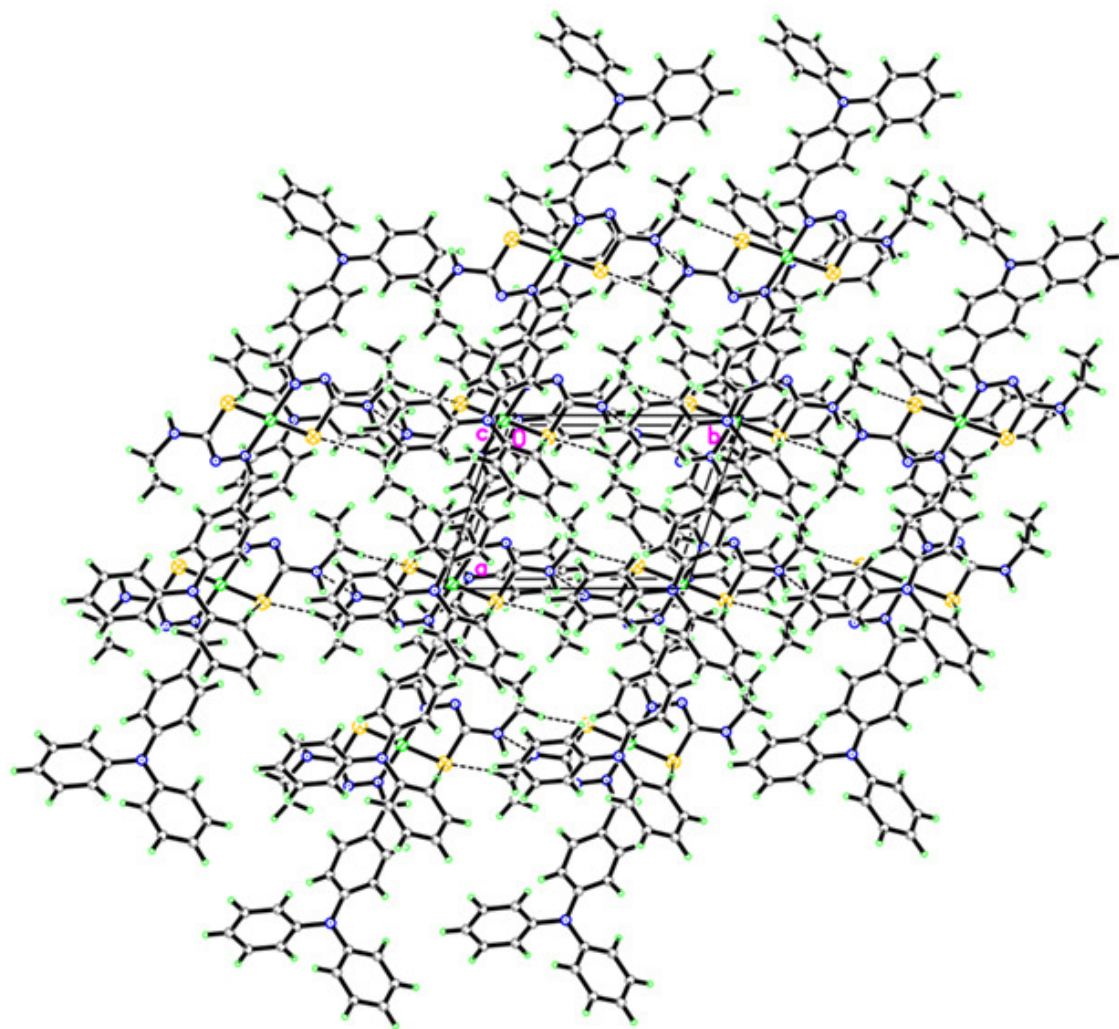


Fig. 2. The crystal packing shows C-H \cdots S interactions of the NiL₂ complex along the *b* axis.

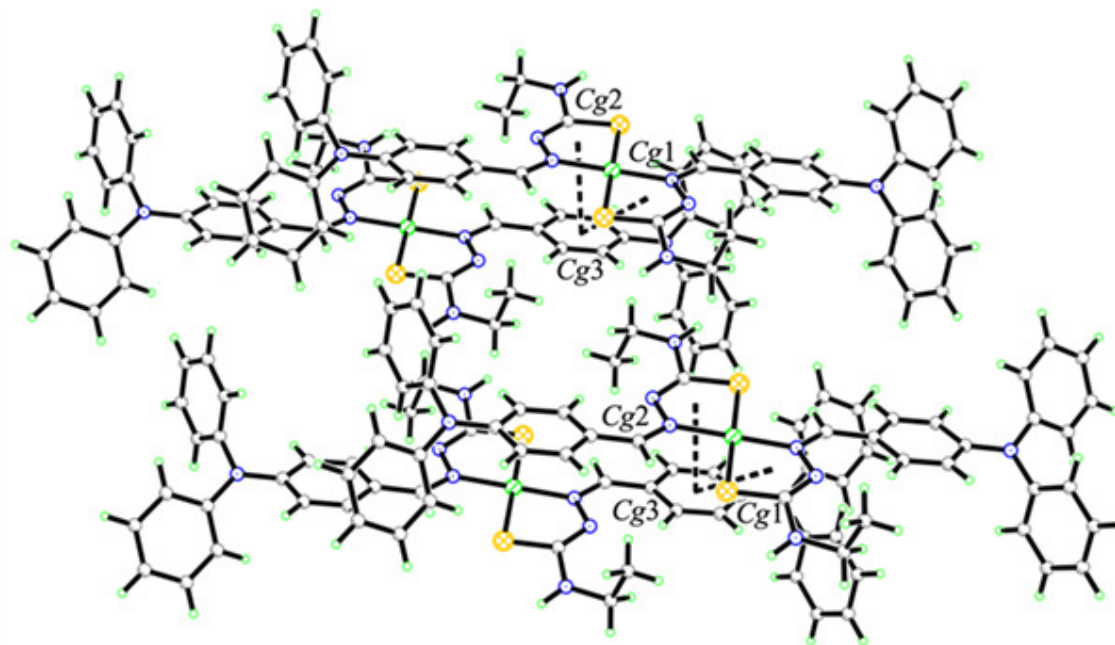


Fig. 3. The crystal packing shows π - π interactions of the NiL₂ complex.

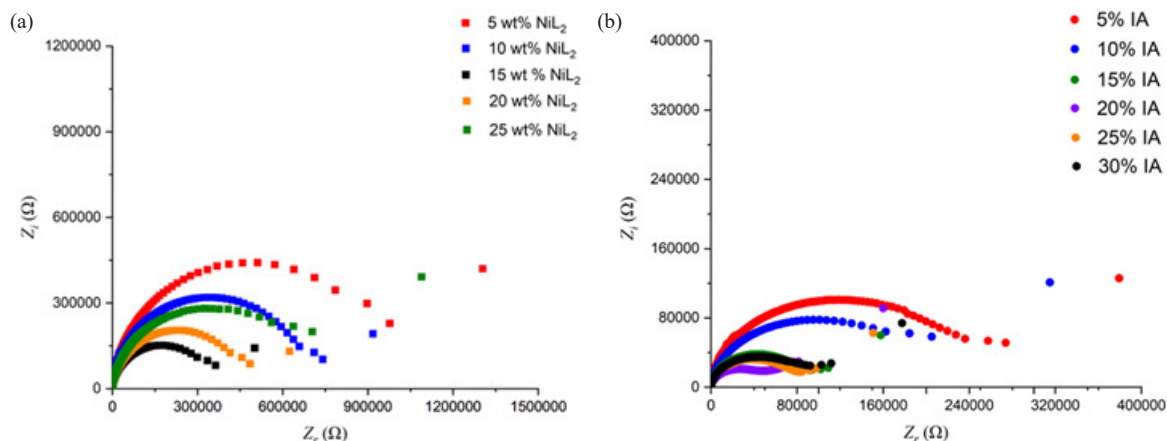


Fig. 4. (a) Nyquist plots for samples with various NiL_2 . (b) Nyquist plots for samples with various IA concentrations at room temperature.

Table 1.

Room temperature conductivity against NiL_2 and IA content.

	Sample designation	Thickness, t (cm)	Bulk resistance, R_b (Ω)	Conductivity, σ (S/cm)
System 1	5 wt% NiL_2	0.010	8.97×10^5	3.55×10^{-9}
	10 wt% NiL_2	0.013	7.10×10^5	5.83×10^{-9}
	15 wt% NiL_2	0.017	2.99×10^5	1.81×10^{-8}
	20 wt% NiL_2	0.022	4.15×10^5	1.69×10^{-8}
	25 wt% NiL_2	0.024	5.60×10^5	1.36×10^{-8}
System 2	5 wt% IA	0.016	2.58×10^5	1.97×10^{-8}
	10 wt% IA	0.019	1.63×10^5	3.71×10^{-8}
	15 wt% IA	0.024	8.47×10^4	9.02×10^{-8}
	20 wt% IA	0.026	5.25×10^4	1.58×10^{-7}
	25 wt% IA	0.028	8.21×10^4	1.09×10^{-7}
	30 wt% IA	0.030	9.01×10^4	1.06×10^{-7}

2) at ambient temperature. The Nyquist plots for both systems have been shown in Fig. 4, respectively. Table 1 presents the ionic conductivity values for all specimens, expressed in S/cm.

In system 1, the incorporation of the newly synthesized dopant, NiL_2 , in concentrations ranging from 5 wt% to 25 wt% reveals a distinct trend of increasing ionic conductivity, with the highest conductivity observed at 15 wt% of the dopant. This enhancement in conductivity can be attributed to the dopant's role in promoting electron mobility within the molecular structure, as the incorporation of the metal center becomes more effective when an electric field is applied to the film (Wu et al., 2024). The improved ion mobility within the dopant molecules contributes to the formation of more efficient ionic conduction pathways. The conductivity reaches its maximum value of $1.81 \times 10^{-8} \text{ S cm}^{-1}$ at 15 wt%, representing an optimal balance where adequate electron pathways are established without excessive obstruction or molecular aggregation. Beyond 15 wt%, however, the conductivity begins to decrease due to the excess dopant, creating a bulkiness of ions on the film, which reduces the ion mobility in the film system (Koopmans et al., 2020).

In system 2, the optimum conductivity of the film (with 15 wt% NiL_2) was further investigated by adding different concentrations of IA, as a proton donor, which protonated the synthesized NiL_2 dopant. The addition of 5 wt% to 20 wt% leads to an increase in conductivity, with the highest value of $1.58 \times 10^{-7} \text{ S cm}^{-1}$. The increase in ionic conductivity that was observed is mainly due to the protonation reaction between the dopant and IA, whereby the protons of IA are transferred to the nitrogen atom (N) of the dopant molecule. The result of this interaction is the creation of hydrogen bonds in the system, which subsequently allows the more effective circulation of electrons throughout the material (Teixeira et al., 2024). The introduction of polymer IA also enhances the concentration of mobile protons in the polymer matrix, which

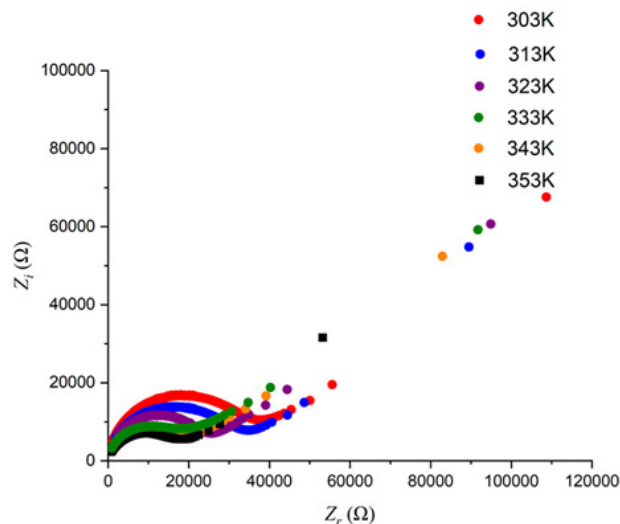


Fig. 5. Nyquist plots for a sample containing 20 wt% IA at different temperatures.

also leads to the overall enhancement of ionic conductivity. This observation is in line with the results of other studies on the topic (Vignesh et al., 2022) that also showed that proton donors like IA can improve conductivity by increasing proton mobility and intermolecular interactions. However, when the IA concentrations were higher than 20%, the ionic conductivity started to decrease as the excess of protons in the system led to aggregation of the dopant, which hinders proton movement and ionic circulation (Luo et al., 2018), forming a thicker film with weak structural integrity.

Fig. 5 shows Nyquist plots for samples with 20 wt% IA at different temperatures. Table 2 summarizes the ionic conductivity values at different temperatures with the R_b derived from the plots in Fig. 5. The results demonstrated that the maximum ionic conductivity for this system was recorded at $4.60 \times 10^{-7} \text{ S cm}^{-1}$ at a temperature of 353 K. This enhancement in conductivity with rising temperature can be attributed to the increased mobility of ions within the CMC polymer matrix, as elevated temperatures reduce the viscosity of the medium and facilitate easier ion transport. As the temperature increases, the polymer chains gain additional energy, which leads to a more dynamic movement of the segments, increasing their flexibility and decreasing the stiffness of the polymer structure (Mohapatra et al., 2015). This allows the ions to move more freely and move closer together (Park et al., 2021). In addition, higher temperatures reduce the intermolecular forces within the matrix, lowering the energy required for ion transport. This combined effect of increased chain flexibility and reduced energy barriers significantly improves the overall ionic conductivity of the system (Zhou et al., 2020).

Table 2.

List of thickness, bulk resistance, and ionic conductivity values for samples containing 20 wt% IA at various temperatures.

Temperature (K)	Thickness, t (cm)	Bulk resistance, R_b (Ω)	Conductivity, σ (S/cm)
303	0.026	3.80×10^4	2.18×10^{-7}
313	0.026	3.50×10^4	2.36×10^{-7}
323	0.026	2.87×10^4	2.88×10^{-7}
333	0.026	2.48×10^4	3.34×10^{-7}
343	0.026	2.10×10^4	3.94×10^{-7}
353	0.026	1.80×10^4	4.60×10^{-7}

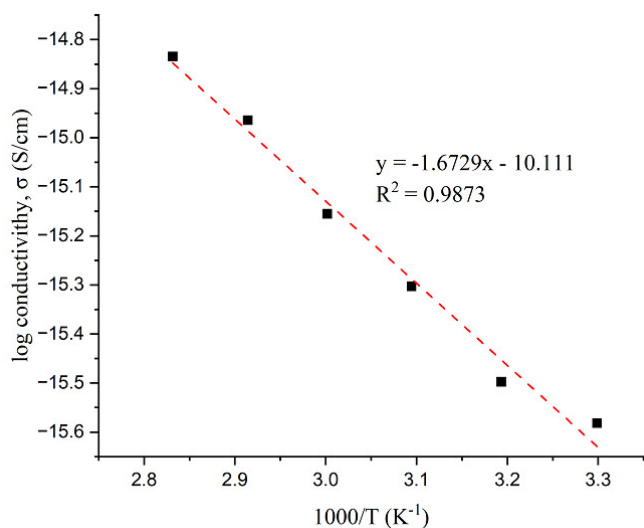


Fig. 6. Temperature-dependent ionic conductivity for samples containing 20 wt% IA.

Fig. 6 shows the linear relationship between the ionic conductivity and the temperature for the sample with 20 wt% IA, which exhibits Arrhenius characteristics. From the slope, the activation energy (E_a) is 0.144 eV, calculated from Eq. 2. This implies that the conduction process in the film has a low thermal energy needed to excite charge carriers. This is indicated by the low activation energy, which suggests a high charge transport efficiency, even at comparatively low temperatures. The $R^2 = 0.9878$ shows that the linear correlation is strong, and the Arrhenius equation is a good approach to explain the temperature-dependent conductivity behavior of the synthesized material. The low thermal activation energy observed suggests that this material may be suitable for use in low-power electronic devices, where minimal energy is required to activate the charge carriers (Lococciolo et al., 2021). This makes the film suitable for various temperature environments in which it can maintain its conductivity even at lower thermal energy levels.

The Nyquist plots shown in Fig. 5 can be translated into an analog circuit model that provides valuable insight into the electrochemical properties of the film system. The equivalent circuit for 20 wt% IA at different temperatures has been shown in Fig. 7. The figure shows that R_b represents the resistance to the ion flow within the mass of the polymer electrolyte. It results from the rearrangement of ions within the free volume of the polymer matrix and indicates how the ions migrate and interact within the materials comprising the film system. The bulk capacitance (C_b) reflects the capacity of the material to retain electrical charge. This can be related to the polarization effects of the

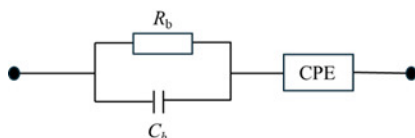


Fig. 7. Equivalent circuit for samples containing 20 wt% IA at various temperatures.

immobile polymer chains, which can affect how charges accumulate and dissipate in the film material. The non-ideal capacitive behavior of the system is considered by the constant phase element (CPE). It is the capacitive effects at the electrode-electrolyte interface and is commonly applied to represent low-frequency spikes (Muchakayala et al., 2017). This equivalent circuit has also been used in previous reports (Ramlli et al., 2022).

4. Conclusions

Synthesis and characterization of the Ni(II) complex containing 4-(diphenylamino)benzaldehyde-4-(ethyl)thiosemicarbazone (NiL_2) as a dopant was carried out. Analytical techniques such as magnetic moment, UV-Vis spectroscopy, elemental analysis, fourier transform infrared (FTIR) spectroscopy, and X-ray crystallography were employed to determine the electronic properties and structure of the complex. The NiL_2 complex adopts a distorted square planar structure with a τ_4 value of 0.107, where it is coordinated by the azomethine ($\text{N}=\text{C}$) and thiosulfur ($\text{C}=\text{S}$) functional groups. The NiL_2 -doped films showed good ionic conductivity when used in CMC films and can be improved by the addition of isophthalic acid (IA) due to the proton interaction with the dopant, which improves the ionic conductivity in the SBE film. As a function of temperature, the conductivity follows the Arrhenius behavior with an activation energy (E_a) of 0.1441 eV, indicating that only a small amount of thermal energy is required to activate the charge carriers.

CRedit authorship contribution statement

W.M. Zuhilmi W.M. Kharul Anwar: experimental studies, data analysis. Uwaisulqarni M. Osman: Concept, design, manuscript preparation, manuscript editing, and manuscript review. Maisara Abdul Kadir: manuscript preparation, manuscript editing, and manuscript review. Khadijah H. Kamarudin: data analysis, manuscript preparation, manuscript editing, and manuscript review. Mohd Ikram Nizam Mohamad Isa: manuscript preparation, manuscript editing, and manuscript review. Suhana Arshad: data analysis, manuscript preparation, manuscript editing, and manuscript review. Siti Nabilla Aliya Mohd Nizar: data analysis, manuscript preparation, manuscript editing, and manuscript review.

Declaration of competing interest

The authors declare that they have no competing financial interests or personal relationships that could have influenced the work presented in this paper.

Data availability

The data used to support the findings of this study are available from the corresponding author upon request.

Declaration of generative AI and AI-assisted technologies in the writing process

The authors confirm that there was no use of Artificial Intelligence (AI)-assisted technology for assisting in the writing or editing of the manuscript and no images were manipulated using AI.

Acknowledgement

This research was sponsored by the Ministry of Higher Education, Malaysia (MOHE), under the Fundamental Research Grant Scheme with reference number FRGS/1/2023/STG05/UMT/02/2 (FRGS-59732).

Supplementary Materials

CCDC: 2404846, contains supplementary crystallographic data for NiL_2 dopant. This data can be obtained free of charge via the Cambridge

Crystallographic Data Centre, 12 Union Road, Cambridge CB2 1EZ, UK; fax: (+44) 1223-336-033; or e-mail through deposit@ccdc.cam.ac.uk. (Supplementary Materials). Supplementary material to this article can be found online at https://dx.doi.org/10.25259/JKSUS_382_2025.

References

- Alam, M.J., Ullah, M.R., Akther, M., 2018. Determination of stability constant of mixed ligand complexes of Ni(II) and Cu(II) metal ions with Diethylenetriamine (DET) and Ethylenediamine(en), Glycine (gly), alpha-Alanine (alpha-ala), Phenylalanine (ph-ala) Oxalic acid (ox), Tyrosin (tyr). *JUSPS-B* 30, 12-19. <https://doi.org/10.22147/jusps-b/300202>
- Anwar, W.M.Z.W.M.K., Osman, U.M., Kamarudin, K.H., Arshad, S., Nizar, S.N.A.M., 2025. Crystal Structure, HOMO-LUMO, Hirshfeld surface analysis and conductivity studies of protonated 4-(diphenylamino)benzaldehyde-4-(ethyl)thiosemicarbazone dopant with carboxymethyl cellulose (CMC). *J Mol Struct* 1340, 142511. <https://doi.org/10.1016/j.molstruc.2025.142511>
- Arafath, M.A., Adam, F., Ahamed, M.B.K., Karim, M.R., Uddin, M.N., Yamin, B.M., Abdou, A., 2023. Ni(II), Pd(II) and Pt(II) complexes with SNO-group thiosemicarbazone and DMSO: Synthesis, characterization, DFT, molecular docking and cytotoxicity. *J Mol Struct* 1278, 134887. <https://doi.org/10.1016/j.molstruc.2022.134887>
- Biswas, C., Vijayan, V., Jyoti Panda, S., Shekhar Purohit, C., Syamala Kiran, M., Ghosh, R., 2024. Anti-cancer and anti-angiogenic activities of some synthetic Ni(II) thiosemicarbazone complexes. *Polyhedron* 252, 116888. <https://doi.org/10.1016/j.poly.2024.116888>
- Bruker, APEX2, SAINT and SADABS, Bruker AXS Inc Madison, (2009) WI, USA.
- Chen, Y., Zhang, Y., Wang, W., Xu, X., Li, Y., Du, M., Li, Z., Zou, Z., 2022. Bandgap engineering and oxygen vacancies of Ni_{1-x}V_xO₅ (x=1, 2, 3) for efficient visible light-driven CO₂ to CO with nearly 100% selectivity. *Solar RRL* 6. <https://doi.org/10.1002/solr.202200099>
- Ekennia, A.C., Ibezim, E.C., Okpareke, O.C., Ibeji, C.U., Anarodu, C.J.O., Babahan, I., Coban, B., Abulhasanov, B., Cömert, F., Ujam, O.T., 2019. Novel 3-Hydroxy-2-naphthoic hydrazone and Ni(II), Co(II) and Cu(II) complexes: Synthesis, Spectroscopic Characterization, antimicrobial, DNA cleavage and computational studies. *Appl Organomet Chem* 33. <https://doi.org/10.1002/aoc.4913>
- El-Shekeil, A., Al-Yusufy, F., Abdulla, A.-H.afeedha., 2010. DC electrical conductivity of polyazomethinthiosemicarbazone metal complexes. *J Appl Polym Sci* 116, 1538-1544. <https://doi.org/10.1002/app.31716>
- Farooq, M.U., Muneer, M., Shahid, A., Rehman, M.A., Ullah, K., Murtaza, G., Iqbal, R., Iqbal, J., Rahimi, M., 2024. Synthesis and characterization of fluorenone derivatives with electrical properties explored using density functional theory (DFT). *Sci Rep* 14, 29015. <https://doi.org/10.1038/s41598-024-80477-0>
- Gaber, A., Refat, M.S., Belal, A.A.M., El-Deen, I.M., Hassan, N., Zakaria, R., Alhomrani, M., Alamri, A.S., Alsanie, W.F., M Saied, E., 2021. New mononuclear and binuclear Cu(II), Co(II), Ni(II), and Zn(II) thiosemicarbazone complexes with potential biological activity: Antimicrobial and molecular docking study. *Molecules* 26, 2288. <https://doi.org/10.3390/molecules26082288>
- Hassan, E.A., Ebrahimi, M.M., Al-Hakimi, A.N., 2024. Synthesis, structural characterization, density functional theory, anticancer, and antimicrobial studies of Ni²⁺ and Cu²⁺ complexes encompassing tridentate ONS-donor azo-thiosemicarbazone. *Appl Organomet Chem* 38. <https://doi.org/10.1002/aoc.7573>
- Khan, T., Raza, S., Lawrence, A.J., 2022. Medicinal utility of thiosemicarbazones with special reference to mixed ligand and mixed metal complexes: A review. *Russ J Coord Chem* 48, 877-895. <https://doi.org/10.1134/s1070328422600280>
- Koopmans, M., Leiviskä, M.A.T., Liu, J., Dong, J., Qiu, L., Hummelin, J.C., Portale, G., Heiber, M.C., Koster, L.J.A., 2020. Electrical conductivity of doped organic semiconductors limited by carrier-carrier interactions. *ACS Appl Mater Interfaces* 12, 56222-56230. <https://doi.org/10.1021/acsami.0c15490>
- Krause, L., Herbst-Irmer, R., Sheldrick, G.M., Stalke, D., 2015. Comparison of silver and molybdenum microfocus X-ray sources for single-crystal structure determination. *J Appl Crystallogr* 48, 3-10. <https://doi.org/10.1107/S1600576714022985>
- Kumar Tarai, S., Tarai, A., Mandal, S., Nath, B., Som, I., Bhaduri, R., Bagchi, A., Sarkar, S., Biswas, A., Ch. Moi, S., 2023. Cytotoxic behavior and DNA/BSA binding activity of thiosemicarbazone based Ni(II) complex: Bio-physical, molecular docking and DFT study. *J Mol Liq* 383, 121921. <https://doi.org/10.1016/j.molliq.2023.121921>
- Lavanya, M., Haribabu, J., Ramaiah, K., Suresh Yadav, C., Kumar Chitumalla, R., Jang, J., Karvembu, R., Varada Reddy, A., Jagadeesh, M., 2021. 2'-Thiophenecarboxaldehyde derived thiosemicarbazone metal complexes of copper(II), palladium(II) and zinc(II) ions: Synthesis, spectroscopic characterization, anticancer activity and DNA binding studies. *Inorganica Chimica Acta* 524, 120440. <https://doi.org/10.1016/j.ica.2021.120440>
- Lococciolo, G., Gupta, S.K., Dechert, S., Demeshko, S., Duboc, C., Atanasov, M., Neese, F., Meyer, F., 2024. Oxygen-donor metalloligands induce slow magnetization relaxation in zero field for a cobalt(II) complex with {CoO₄} Motif. *Inorg Chem* 63, 5652-5663. <https://doi.org/10.1021/acs.inorgchem.4c00054>
- Luo, F., Zhang, Q., Yang, Z., Guo, L., Yu, X., Qu, K., Ling, Y., Yang, J., Cai, W., 2018. Fabrication of stable and well-connected proton path in catalyst layer for high temperature polymer electrolyte fuel cells. *ChemCatChem* 10, 5314-5322. <https://doi.org/10.1002/cctc.201801256>
- Mohapatra, S.R., Tsuruoka, T., Krishnan, K., Hasegawa, T., Aono, M., 2015. Effects of temperature and ambient pressure on the resistive switching behaviour of polymer-based atomic switches. *J Mater Chem C* 3, 5715-5720. <https://doi.org/10.1039/c5tc00842e>
- Muchakayala, R., Song, S., Gao, S., Wang, X., Fan, Y., 2017. Structure and ion transport in an ethylene carbonate-modified biodegradable gel polymer electrolyte. *Polym Test* 58, 116-125. <https://doi.org/10.1016/j.polymertesting.2016.12.014>
- Muthuramalingam, S., Sankaralingam, M., Velusamy, M., Mayilmurugan, R., 2019. Catalytic conversion of atmospheric CO₂ into organic carbonates by nickel(II) complexes of diazepane-based N4 ligands. *Inorg Chem* 58, 12975-12985. <https://doi.org/10.1021/acs.inorgchem.9b01908>
- Osman, U.M., Silvarajoo, S., Kamarudin, K.H., Tahir, M.I.M., Kwong, H.C., 2021. Ni(II) complex containing a thiosemicarbazone ligand: Synthesis, spectroscopy, single-crystal X-ray crystallographic and conductivity studies. *J Mol Struct* 1223, 128994. <https://doi.org/10.1016/j.molstruc.2020.128994>
- Osman, U.M., Silvarajoo, S., Noor Hassim, M.F., Arshad, S., Anizaim, A.H., Abdul Razak, F.I., 2021. Synthesis, X-ray structure, hirshfeld surface analysis, DFT calculations, and molecular docking studies of nickel(II) complex with thiosemicarbazone derivative. *Bioinorg Chem Appl* 2021, 5536902. <https://doi.org/10.1155/2021/5536902>
- Park, J., Staiger, A., Mecking, S., Winey, K.I., 2021. Structure-property relationships in single-ion conducting multiblock copolymers: A phase diagram and ionic conductivities. *Macromolecules* 54, 4269-4279. <https://doi.org/10.1021/acs.macromol.1c00493>
- Phi, T.L., Nguyen, S.T., Van Hieu, N., Palomar-Pardavé, M., Morales-Gil, P., Le Manh, T., 2022. Insights into electrocatalysis and electrodeposition of nickel from a non-aqueous solvent based on NiCl₂·6H₂O dissolved in ethylene glycol. *Inorg Chem* 61, 5099-5111. <https://doi.org/10.1021/acs.inorgchem.2c00127>
- Ramli, M.A., Mohamad ISA, M.I.N., Kamarudin, K.H., 2022. 2-hydroxyethyl cellulose-ammonium thiocyanate solid biopolymer electrolytes: Ionic conductivity and dielectric studies. *JSSM* 17, 121-132. <https://doi.org/10.46754/jssm.2022.07.009>
- Rajeev, A., Thomas, A.T., Das, A., Sankaralingam, M., 2024. C-H bond activation facilitated by nickel(II) complexes having mighty claws. *Eur J Inorg Chem* 27. <https://doi.org/10.1002/ejic.202400205>
- Rathinam, M., Vijayan, P., Balasubramanian, S., Ponnusamy, S., SaravanaVadivu, A., Abbas, M., Balakrishnan, B.B., 2024. Nicotine sensing behavior of nickel(II) complexes catalyzed oxidation and coupling reactions. *Heliyon* 10, e27102. <https://doi.org/10.1016/j.heliyon.2024.e27102>
- Sarker, D., Hossen, M. F., Kudrat-E-Zahan, M., Haque, M.M., Zamir, R., Asraf, M.A., 2020. Synthesis, characterization, thermal analysis and antibacterial activity of Cu (II) and Ni(II) complexes with thiosemicarbazone derived from thiophene-2-aldehyde. *J Mater Sci Res Rev* 3, 64-74. <https://journaljmsrr.com/index.php/JMSRR/article/view/92>
- Seifunnisha, O., Swathi, R., Shanthi, J., 2021. Non-wettable antibacterial thin film: PS/Aloe vera and PS/Acalypha indica. *Polymers Polymer Composites* 29, S622-S630. <https://doi.org/10.1177/09673911211017869>
- Sheldrick, G.M., 2015. Crystal structure refinement with SHELXL. *Acta crystallogr C Struct Chem* 71, 3-8. <https://doi.org/10.1107/S2053229614024218>
- Sohaimy, M.I.H., Isa, M.I.N., 2022. Proton-conducting biopolymer electrolytes based on carboxymethyl cellulose doped with ammonium formate. *Polymers (Basel)* 14, 3019. <https://doi.org/10.3390/polym14153019>
- Tamer, Ömer, Dege, N., Avci, D., Atalay, Y., 2023. The static and frequency-dependent second- and third-order nonlinear optical properties of Zn(II) and Ni(II) complexes of 4-methoxypyridine-2-carboxylic acid: A detailed experimental and theoretical study. *Appl Organomet Chem* 37. <https://doi.org/10.1002/aoc.7206>
- Teixeira, F.C., Teixeira, A.P.S., Rangel, C.M., 2024. New triazinephosphonate dopants for Nafion proton exchange membranes (PEM). *Beilstein J Org Chem* 20, 1623-1634. <https://doi.org/10.3762/bjoc.20.145>
- Vignesh, D., Sonu, B.K., Rout, E., 2022. Factors constituting proton trapping in BaCeO₃ and BaZrO₃ perovskite proton conductors in fuel cell technology: A review. *Energy Fuels* 36, 7219-7244. <https://doi.org/10.1021/acs.energyfuels.2c00650>
- Wu, Y., Salamat, C.Z., León Ruiz, A., Simafranca, A.F., Akmanşen-Kalayci, N., Wu, E.C., Doud, E., Mehmedović, Z., Lindemuth, J.R., Phan, M.D., Spokoyny, A.M., Schwartz, B.J., Tolbert, S.H., 2024. Using bulky dodecaborane-based dopants to produce mobile charge carriers in amorphous semiconducting polymers. *Chem Mater* 36, 5552-5562. <https://doi.org/10.1021/acs.chemmater.4c00502>
- Zangrando, E., Islam, M.T., Islam, M.A.A.A., Sheikh, M.C., Tarafder, M.T.H., Miyatake, R., Zahan, R., Hossain, M.A., 2015. Synthesis, characterization and bio-activity of nickel(II) and copper(II) complexes of a bidentate NS Schiff base of S-benzyl dithiocarbamate. *Inorganica Chimica Acta* 427, 278-284. <https://doi.org/10.1016/j.ica.2014.12.014>
- Zhang, Y., Du, M.X., La, Y.T., Yan, Y.J., Dong, W.K., 2024. Synthesis, structural characterizations and theoretical calculations of the Ni(II) complex based on a novel salamo-salen-salamo-type hybrid ligand. *J Mol Struct* 1296, 136841. <https://doi.org/10.1016/j.molstruc.2023.136841>
- Zhou, X., Wang, Z., Epszstein, R., Zhan, C., Li, W., Fortner, J.D., Pham, T.A., Kim, J.H., Elimelech, M., 2020. Intrapore energy barriers govern ion transport and selectivity of desalination membranes. *Sci Adv* 6, eabd9045. <https://doi.org/10.1126/sciadv.abd9045>